Monthly Notices of the ROYAL ASTRONOMICAL SOCIETY

MNRAS **516,** 5655–5673 (2022) https://doi.org/10.1093/mnras/stac2588
Advance Access publication 2022 September 15

AlH lines in the blue spectrum of Proxima Centauri

Yakiv V. Pavlenko,[1,2,3,4]★ Jonathan Tennyson [5]★ Sergei N. Yurchenko [5] Mirek R. Schmidt,[2]★ Hugh R. A. Jones,[4] Yuri Lyubchik[1] and A. Suárez Mascareño [3]

[1]*Main Astronomical Observatory, Academy of Sciences of the Ukraine, 27 Zabolotnoho, Kyiv 03143, Ukraine*
[2]*Nicolaus Copernicus Astronomical Center, Polish Academy of Sciences, Rabiańska 8, PL-87-100 Toruń, Poland*
[3]*Instituto de Astrofísica de Canarias (IAC), Calle Vía Láctea s/n, E-38200 La Laguna, Tenerife, Spain*
[4]*Centre for Astrophysics Research, University of Hertfordshire, College Lane, Hatfield AL10 9AB, UK*
[5]*Department 'of Physics and Astronomy, University College London, London WC1E 6BT, UK*

Accepted 2022 September 5. Received 2022 September 5; in original form 2022 June 1

ABSTRACT

The recently computed ExoMol line lists for isotopologues of AlH are used to analyse the blue spectrum (4000–4500 Å) of Proxima Cen (M5.5 V). Comparison of the observed and computed spectra enables the identification of a large number of ^{27}AlH lines of the A $^1\Pi$ –X $^1\Sigma^+$ band system: The spectral range covering 1-0, 0-0, and 1-1 bands are dominated by clearly resolved AlH lines. We reveal the diffuse nature of transitions close to the dissociation limit which appears in the form of increasingly wider (up to 5 Å) and shallower (up to the continuum confusion limit) AlH line profiles. The predicted wavelengths of AlH diffuse lines are systematically displaced. The effect of broadening by predissociation states on the line profiles is included by increasing the radiative damping rate by up to 5 orders of magnitude. We determine empirical values of damping rates for a number of the clean 0-0 Q-branch transitions by comparing the observed and synthetic stellar spectra. We find excellent agreement between our damping rates and lifetimes available in the literature. A comparison of ^{27}Al^{1}H ExoMol and REALH spectra shows that the observed spectrum is better described by the ExoMol line list. A search for ^{26}Al^{1}H lines in the Proxima Cen spectrum does not reveal any notable features; giving an upper limit of ^{27}Al^{1}H /^{26}Al^{1}H >100.

Key words: line: identification – molecular data – opacity – stars: atmospheres – stars: individual: Proxima Cen – stars: late-type.

1 INTRODUCTION

Aluminum is one of the commoner interstellar metallic elements, with a cosmic abundance of A(Al) = −5.53 on a scale where the sum of all abundances equals 1.0 (Anders & Grevesse 1989). ^{27}Al comprises 100 per cent of all natural aluminum, at least in the Solar system (Lodders, Palme & Gail 2009). Spectra of aluminum-containing molecules, i.e. AlNC, AlF, and AlCl have been observed in the envelopes around the C-rich asymptotic giant branch stars (Cernicharo & Guelin 1987; Ziurys et al. 2002) and the Mira-variable *o* Ceti (Kamiński et al. 2016)). AlOH, a new interstellar molecule, was detected towards the envelope of VY Canis Majoris (VY CMa), an oxygen-rich red supergiant, by Tenenbaum & Ziurys (2010). Three rotational transitions of AlOH were observed using the Arizona Radio Observatory (ARO): The $J = 9 \rightarrow 8$ and $J = 7 \rightarrow 6$ lines at 1 mm were measured with the ARO Submillimeter Telescope, while the $J = 5 \rightarrow 4$ transition at 2 mm was observed with the ARO 12 m antenna on Kitt Peak. Kamiński et al. (2018) reported observations of millimetre-wave rotational lines of the isotopologue of aluminum monofluoride that contains the radioactive isotope (^{26}AlF). This emission was observed towards CK Vul, which is thought to be a remnant of a stellar merger. Kamiński, Schmidt & Menten (2013) reported the first identification of the optical bands of the B $^1\Sigma^+$ – X $^1\Sigma^+$ system of AlO in the spectrum of the red supergiant VY CMa. Bessell (2011) identified the (0,0) and (1,1) AlH A $^1\Pi$ –X $^1\Sigma^+$ bands in the spectrum of Proxima Cen.

Surprisingly, thus far, the simplest possible molecule containing aluminum, AlH has yet to be detected in interstellar gas. In part, this is because cold AlH is harder to detect due to its small reduced mass, which causes its rotational transitions to occur in the submillimetre region. Unfortunately, the 1-0 transition at 423.9 GHz lies on a shoulder of a saturated telluric line, which makes its detection problematic. The non-detection of interstellar AlH is somewhat surprising, given the well-documented presence of this molecule in the photospheres of χ Cygni and other stars (Herbig 1956; Johnson & Sauval 1982), as well as in the sunspots (see Wallace, Hinkle & Livingston 2000, Karthikeyan, Rajamanickam & Bagare 2010, and reference therein).

The AlH electronic system A $^1\Pi$ – X $^1\Sigma^+$ has been extensively studied in the laboratory, see Zhu, Shehadeh & Grant (1992) and Ram & Bernath (1996). Recently, Halfen & Ziurys (2014) carried out sophisticated measurements of the $J = 2 \leftarrow 1$ rotational transition of AlH (X $^1\Sigma^+$) near 755 GHz and the $J = 4 \leftarrow 3$ line of AlD (X $^1\Sigma^+$) near 787 GHz and to aid terahertz direct absorption analysis. The ro-vibration spectra of the X $^1\Sigma^+$ state of both AlH and AlD have been recorded and analysed by numerous groups, as well, using laser-diode and Fourier transform infrared methods, see Ito et al. (1994), and White, Dulick & Bernath (1993) who measured a wide range of

★ E-mail: yp@mao.kiev.ua (YVP); j.tennyson@ucl.ac.uk (JT); schmidt@ncac.torun.pl (MRS)

rovibrational lines of AlH, from $v = 1 - 0$ to $v = 5$–4, with high precision. Qin, Bai & Liu (2021) discussed the photodissociation of AlH, mainly for electronic bands in the far-UV. High-resolution spectroscopic studies allow to specify rotational and vibrational spectroscopic parameters to be derived for the AlH molecule, see Yurchenko et al. (2018) for more details and an extensive list of references to laboratory work.

The upper state of AlH system $A\,^1\Pi - X\,^1\Sigma^+$ becomes predissociative with rotational excitation (Baltayan & Nedelec 1979). The first indications of this effect in AlH was presented by Farkas (1931) in absorption and by Bengtsson & Rydberg (1930) in emission. It appears when the energy of the upper rotational (predissociating) state is higher then the dissociation limit of its electronic state. The bound state is then in fact quasi-bound, because it may convert to continuum state by tunneling through the centrifugal barrier. As a result, the molecule dissociates. If the barrier is not too high then it will decrease the lifetime of the level, τ, according to the formula (Baltayan & Nedelec 1979):

$$1/\tau = 1/\tau_{\rm radiative} + 1/\tau_{\rm dissociative}. \quad (1)$$

For AlH, predissociation can totally dominate the the lifetime of the highest rotational states. The observable consequences are different in case of emission or absorption. In emission, the decay of the upper quasi-bound state goes mainly by the radiationless process, i.e, without photon emission. The emission spectrum is then limited to some maximal rotational number, breaking off sharply. In absorption, radiative transitions to quasi-bound states are preserved, but because the lifetime of quasi-bound states is very short, the damping rate of these states due to the uncertainty principle is high and the lines may be very broad, as will be seen below.

The purpose of this paper is to identify and analyse the AlH lines in the spectrum of Proxima Cen (M5.5V) using a comparison between theoretical and observed spectra. The star is an old M-dwarf that burned its deuterium and lithium a long-time ago.

Proxima Cen is a member of α Cen triple system, one of its aliases is α Cen C. The two other components show a weak overabundance (0.2 dex) of metals in their atmospheres, which is different for A and B, see Casali et al. (2020), Steinmetz et al. (2020), and references therein.

Much of the optical spectrum of the Proxima Cen is dominated by TiO and VO bands, but in the blue part of spectrum, it is largely dominated by atomic absorption (Pavlenko et al. 2017). Proxima Cen shows a high level of activity (see Pavlenko et al. 2017, 2019, and references therein). For example, in March 2016 the Evryscope team observed that a superstrong naked-eye-brightness superflare occurred in the atmosphere of Proxima Cen (Howard et al. 2018) releasing a bolometric energy of $10^{33.5}$ erg. The optical flux increased by a factor of about 68 during this superflare. Over the last few years, the Evryscope team has recorded a few dozen other large Proxima Cen flares. Recently, an extreme flaring event from Proxima Cen was observed on 2019 May 1 by the Australian Square Kilometre Array Pathfinder, Atacama Large Millimeter/submillimeter Array (ALMA), *Hubble Space Telescope* (*HST*), Transiting Exoplanet Survey Satellite, and the du Pont Telescope. In the millimeter and FUV, this flare is the brightest ever detected, brightening by a factor of >1000 and $>14\,000$ as seen by ALMA and *HST*, respectively (MacGregor et al. 2021). These mighty stellar flares give rise to high-energy cosmic rays that can drive large amounts of nucleosynthesis in stellar atmospheres, including the formation of the radioactive ^{26}Al atoms with a half-life of $t_{1/2} = 7.2 \times 10^5$ yr. Indeed, high-energy cosmic rays may induce nuclear reactions on materials to produce ^{26}Al via of the ^{28}Si(d,α)^{26}Al channel, as was confirmed experimentally by Araujo-Escalona et al. (2015, 2016). The sources of ^{26}Al in the Galaxy is an important issue in nuclear astrophysics, see Palmerini et al. (2020) and references therein. Here, we attempt to detect ^{26}Al^{1}H in Proxima Cen.

2 OBSERVED SPECTRUM

We retrieved the spectrum of Proxima Cen from the HARPS ESO public data archive. HARPS (Mayor et al. 2003) has a resolving power $R \sim 115\,000$ over the spectral range from 3780 to 6810 Å. Our analysis used all available reduced wavelength-calibrated spectra produced by the HARPS pipeline. Details of the data-reduction procedure were described by Pavlenko et al. (2017). We corrected every spectrum for the velocity of the star and created a high-signal-to-noise ratio spectrum by co-adding all the available spectra. Some remnants of the calibration lines of varying intensity form artifacts in the final spectrum. They appear irregularly in intervals of 32–37 Å in the form of clusters of emission features. As a result, narrow spectral ranges of the width of about 1.7 Å were excluded from the analysis. As these may influence the process of automatic tracing of continuum, in selected spectral ranges the continuum tracing was performed manually after removing these artefacts.

Unfortunately, the HARPS pipeline does not provide properly calibrated fluxes. This means that even for comparatively short spectral ranges we should compare two F_λ with different flux slopes $\partial F_\lambda/\partial\lambda$.

To simplify the analysis, we reduced the observed spectra to the local pseudo-continuum level using the program Rassine (Cretignier et al. 2020), see top panel of Fig. 1. Strictly speaking, this procedure is correct only in the spectral ranges of weak molecular bands, where one can recognize the 'true continuum'. A haze of TiO lines dominates for $\lambda > 4300$ Å, so the definition of the 'local continuum' must be used here with certain reservations. In practice, we use the local pseudo-continuum here too.

The emission details seen in the observed spectrum of Proxima Cen are real emission lines, see Pavlenko et al. (2017), but they are beyond the scope of this paper. Rassine's pseudo-continuum is used to evaluate the reference level of the flux, which can be compared with the theoretical predictions.

3 PROCEDURE

Computation of the theoretical spectra was performed using program `Wita6`, see Pavlenko (1997), Pavlenko, Zapatero Osorio & Rebolo (2000), Pavlenko et al. (2017). Line-by-line computations by `Wita6` allow one to account for blending effects. Instrumental broadening as well as broadening by rotation are implemented for the computed spectra. We used `WITA6` to compute the synthetic spectra in the framework of the classical approximations (1D, LTE, hydrodynamic equilibrium, no internal sources of energy generation/sinks).

3.1 Continuum opacity

In our procedure for the computation of synthetic spectra, we accounted for all known continuum opacities, including continuum scattering that are adopted for late-type stellar atmospheres in ATLAS9-12 (Kurucz 2014).

3.2 Atomic and molecular line lists

Atomic lines dominate at the bluer spectral range of interest, i.e. at $<$ 4250 Å, a tail of the α-band system of TiO and comparatively weak

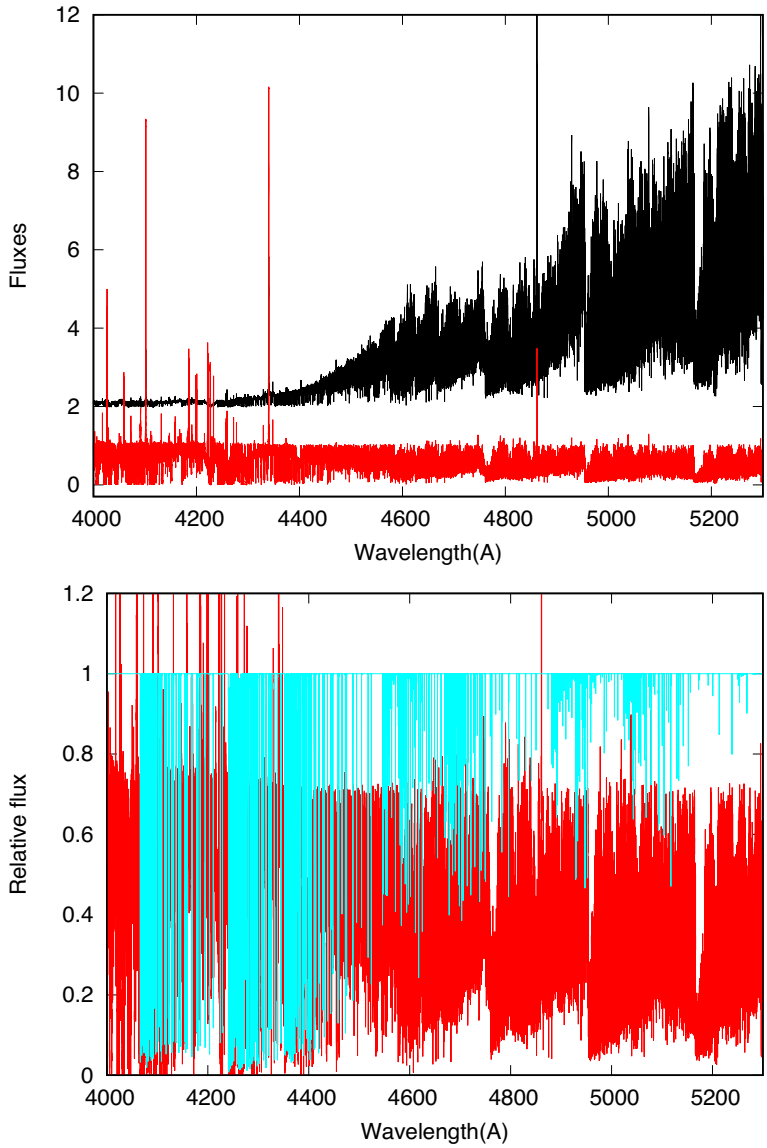

Figure 1. Top panel: Observed HARPS *s1d* spectrum of Proxima Cen (black line) and the same spectrum reduced to continuum/pseudo-continuum (red line). Bottom panel: A comparison of the theoretical R_f (cyan line) and reduced to pseudo-continuum observed spectrum (red line).

lines of A-X system of MgH present here, as well, see Pavlenko (2014) and http://www.mao.kiev.ua/staff/yp/Results/M-stars/mb.htm.

3.2.1 *WYLLoT $^{26}Al^1H$ and $^{27}Al^1H$ line lists*

We use the computed WYLLoT lists of ^{26}Al^{1}H and ^{27}Al^{1}H lines (Yurchenko et al. 2018) which forms part of the ExoMol database (Tennyson et al. 2020). The line list spans two electronic states $X\,^1\Sigma^+$ and $A\,^1\Pi$. An adiabatic model was used by the ExoMol group to model the shallow potential energy curve of the $A\,^1\Pi$ state, which has a strong predissociative character with only two bound vibrational states. Rotation–vibration resolved lists for the ground $X\,^1\Sigma^+$ and $A\,^1\Pi$ excited electronic states of AlH were obtained by solving the nuclear-motion Schrödinger equation using the program Duo (Yurchenko et al. 2016) in conjunction with empirical potential energy curves and couplings. That way, high-temperature line lists plus partition functions and lifetimes were generated for three isotopologues ^{27}AlH, ^{27}AlD, and ^{26}AlH using *ab initio* (transition) dipole moments. Where available, the calculated (empirical) energies of ^{27}AlH and ^{27}AlD were replaced by experimentally determined values using the MARVEL (measured active rotation–vibration energy levels) methodology (Furtenbacher, Császár & Tennyson 2007). The line lists cover both the X-X and A-X band systems and were downloaded from the ExoMol website (www.exomol.com).

To work in the framework of the 'astrophysical' convention (Pavlenko, Yurchenko & Tennyson 2020), i.e. reduced account of the nuclear spin degeneracy, we scaled the ExoMol statistical factor g_i and partition function $Q(T)$:

$$g_{\rm i} f_{\rm if}^{\rm (astro)} = \frac{g_{\rm i} f_{\rm if}^{\rm (phys)}}{\bar{g}^{\rm (ns)}}, \tag{2}$$

$$Q^{\rm (astro)} = \frac{Q^{\rm (phys)}}{\bar{g}^{\rm (ns)}}. \tag{3}$$

where $\bar{g}^{\rm (ns)}$ is the 'total' nuclear spin degeneracy. In the case of ^{27}Al^{1}H , ^{27}Al, and ^{1}H have nuclear spin degeneracy of 6 and 2,

Table 1. Dissociation constants for Al contained molecules accounted in this paper, see equation (5).

Molecule	D_0 /eV	b	c	d	e	h
AlH	3.160	0.4684E + 02	0.2238E-02	0.4873E-06	0.5607E-10	0.2425E-14
AlS	3.817	0.4664E + 02	0.1771E-02	0.3351E-06	0.3320E-10	0.1240E-14
AlO	4.889	0.4817E + 02	0.2438E-02	0.4827E-06	0.5331E-10	0.2270E-14
AlF	6.854	0.4744E + 02	0.1771E-02	0.3223E-06	0.3120E-10	0.1148E-14
AlCl	5.075	0.4672E + 02	0.1701E-02	0.2726E-06	0.2530E-10	0.9247E-15
Al_2O_3	20.108	0.2005E + 03	0.1182E-01	0.2905E-05	0.4139E-09	0.2363E-13
AlOH	9.977	0.9727E + 02	0.4470E-02	0.9826E-06	0.1121E-09	0.4709E-14
AlO_2	8.329	0.9826E + 02	0.4021E-02	0.5717E-06	0.4122E-10	0.1105E-14

respectively, so the total nuclear spin degeneracy $\bar{g}^{(\mathrm{ns})} = 12$. For ^{26}Al $\bar{g}^{(\mathrm{ns})} = 11$, giving $\bar{g}^{(\mathrm{ns})} = 22$ for ^{26}Al^{1}H .

3.2.2 *REALH ^{27}Al^{1}H list*

We also used the REALH line list ^{27}Al^{1}H of Szajna & Zachwieja (2009). This line list was obtained from the analysis of the high-resolution emission spectrum of the A $^1\Pi$–X $^1\Sigma^+$ system of ^{27}Al^{1}H observed in the 18 000–25 000 cm^{-1} spectral region using a conventional spectroscopic technique. In total Szajna & Zachwieja (2009) measured and analysed 163 transitions from six bands, 0–0, 0–1, 1–0, 1–1, 1–2, and 1–3. To get the reasonable fit, they combined these data with available high-resolution measurements of the vibration-rotation bands by White et al. (1993). This procedure allowed them to fit molecular constants for the A$^1\Pi$ and X$^1\Sigma^+$ states of ^{27}Al^{1}H . Interestingly, a weak local perturbations was revealed in the $v = 1$ vibration level of the A$^1\Pi$ state at $J = 5$. This may be caused by the interaction with the a $^3\Pi$ state.

Conversely, the ExoMol spectoscopic model used for the WYLLoT line list did not include the dark a$^3\Pi$ state included in its spectroscopic model and should, in principle, be also affected by the omission of possible perturbations. However, the ExoMol A $^1\Pi$ $v = 1$ state energies in this region were replaced by experimental values and therefore should be independent from any theoretical artifacts.

3.2.3 *Other line lists*

We accounted for other absorbers in our model computations as well. In addition to TiO provided by ExoMol (McKemmish et al. 2019), molecular bands of CaH, MgH, and other hydrides was taken from the Kurucz database (Kurucz 2011), and atomic line list was taken from the VALD (Ryabchikova & Pakhomov 2015).

3.3 AlH dissociation equilibrium

In the Kurucz (1970) treatment of dissociation, the Golberg–Waage equation is given by

$$\frac{n_{1,2,\ldots l}^{p+}}{\prod_i^l n_i} = \frac{Q_{1,2\ldots l} \times y(m_{123\ldots l}, T) \times (2 \times y(m_{\mathrm{e}}, T))^p}{\prod_i^l (Q_i \times y(m_i, T))} \times \exp\left(-\frac{D_{1,2,\ldots l}}{kT}\right), \quad (4)$$

where m_i, n_i^{p+} and Q_i are the mass, number density, and partition function of the i −th specie with the positive change p, respectively; $D_{123..l}$ is the dissociation energy of molecule 1, 2, 3...l, k is the Boltzmann constant, and and T is the temperature; $y(m_i, T) = (2 \times \pi \times m_i \times k \times T/h^2)^{3/2}$. The equation 4 can be written in the form Kurucz (1970):

$$\frac{\prod_i^l n_i}{n_{1,2,\ldots l}} = \exp[-D_{1,2,\ldots l}/kT + g(T)], \quad (5)$$

where

$$g(T) = b - c \times T + d \times T^2 - e \times T^3 + h \times T^4) + \frac{3}{2}(l - p - 1)\ln T. \quad (6)$$

Other forms can be found in e.g. Sauval & Tatum (1984) or Tsuji (1973).

For AlH, we use a dissociation energy of $D_0 = 3.16$ eV (Baltayan & Nedelec 1979); for more information, see Yurchenko et al. (2018) and references therein. Other constants were computed with the partition function $Q(T)/\bar{g}^{(\mathrm{ns})}$, where $Q(T)$ was provided by Yurchenko et al. (2018). New constants for AlH and constants for other molecules used in the computations of the ionisation-dissociation equilibrium are shown in Table 1. Constants for molecules other than AlH were recomputed in the new format using data of Gurvich, Veits & Alcock (1989) or Tsuji (1973).

3.4 Synthetic spectra

To compute theoretical spectra using `Wita6`, we employed the BT–Settl model atmosphere (Allard 2014) with T_{eff}/logg/[Fe/H] = 2900/4.5/0, as determined in our previous paper, see Pavlenko et al. (2017). We adopted the solar abundances of Anders & Grevesse (1989). Voigt functions were used to describe the profile of the absorption coefficient of every line accounted for. For atomic lines, we took damping constants c_2, c_4, and c_6 from the VALD database. Pressure damping dominates in cool and dense atmospheres of late-type dwarfs, see Burrows & Volobuyev (2003). If the damping constants are missing in VALD then we compute them in the Unsold (1955) approximation. We used the same scheme for molecular lines, as well. Synthetic spectra were computed with a wavelength step of 0.01 Å. Detailed investigations showed that microturbulent velocities are lower for cooler dwarfs of earlier spectral classes G-K, see Sitnova et al. (2015); we adopted the microturbulent velocity $V_t = 1$ km/s. Strictly speaking, this parameter is not of critical importance in the framework of this paper, because most AlH lines are strong or even saturated in the Proxima Cen spectrum, strong lines show rather marginal response on changes V_t. Furthermore, computations by Pavlenko et al. (2017) did not reveal any notable rotational velocities ($v \sin i$) of Proxima Cen, therefore the theoretical spectra were convolved with a pure Gaussian profile in order to model the instrumental broadening, see the next subsection. Computations by Pavlenko et al. (2017) did not reveal any notable rotational velocities ($v \sin i$) of Proxima Cen: This is expected. Proxima's rotation period

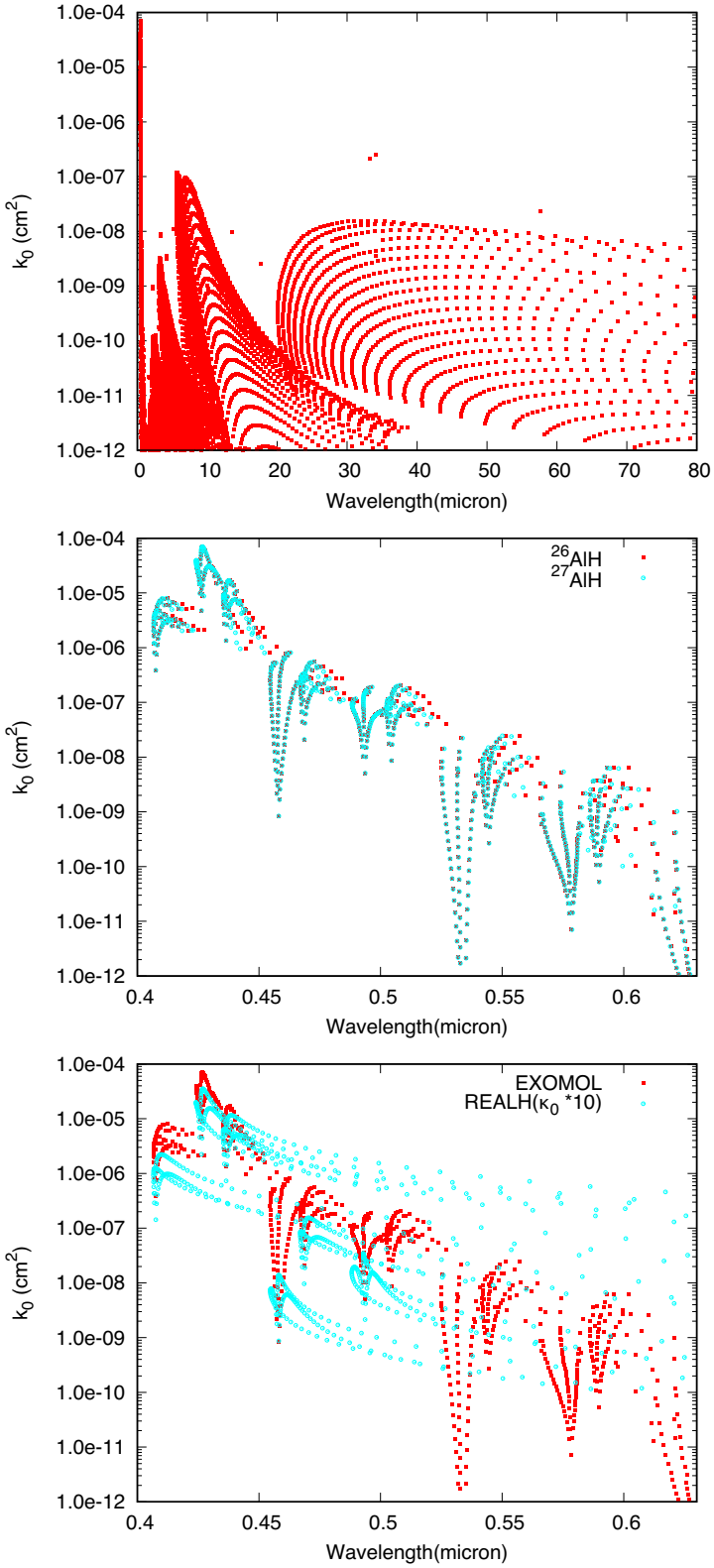

Figure 2. Top panel: Computed absorption coefficients k_0 per $^{27}Al^1H$ molecule across a wide spectral range. Middle panel: Red and cyan lines, depict k_0 of $^{27}Al^1H$ and $^{26}Al^1H$ line absorption, respectively, on a larger scale in the optical. Bottom panel: Red and cyan lines depict the k_0 of $^{27}Al^1H$ of ExoMol and REALH line absorption, respectively. To get line strengths for both line lists on one scale, we increase REALH *gf*s by a factor of 10.

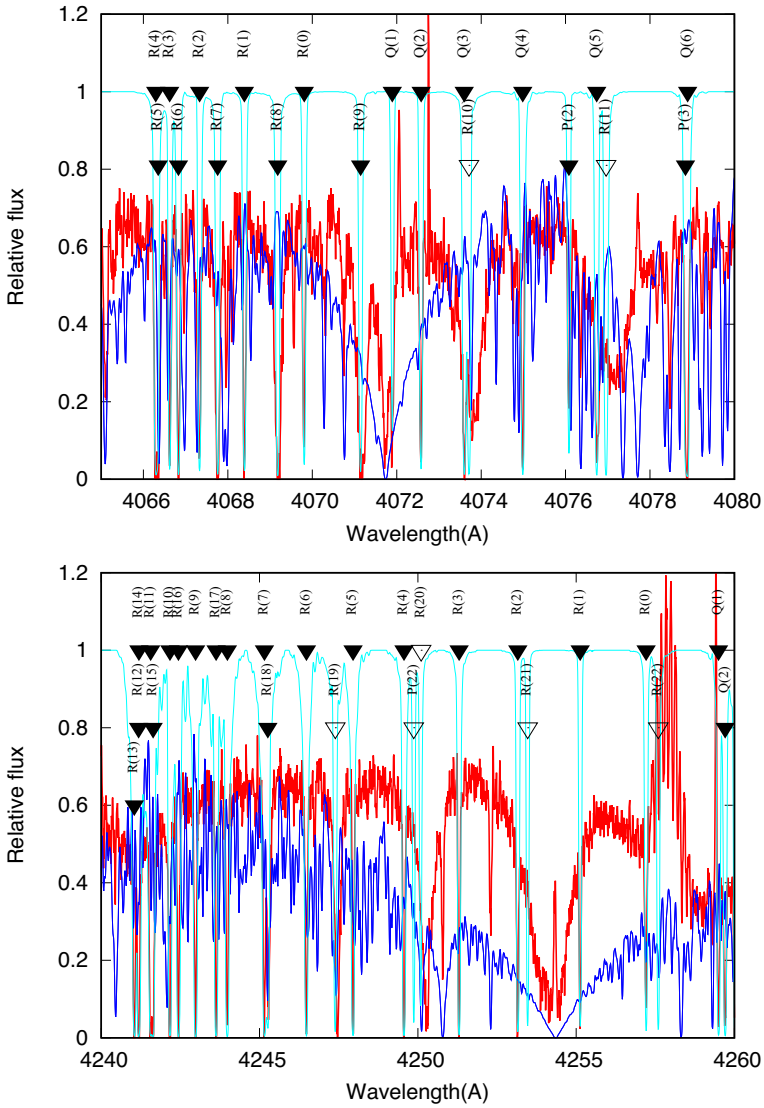

Figure 3. The spectrum of Proxima Cen (red line) reduced to a pseudo-continuum. Two selected spectral ranges covering the band heads of the $A\,^1\Pi - X\,^1\Sigma^+$ (1-0) and (0-0) bands are shown in the top and bottom panels, respectively. The blue line represents the theoretical spectrum computed without AlH lines. The cyan line shows the contribution of AlH lines to the synthetic spectrum (R_f – see explanation in the text). Clear absorption lines of AlH are marked by ▼. AlH lines involving higher J levels misplaced in the theoretical spectrum are labelled by ▽ (see Section 4.2.2). Issues with lines that are too broad in the computed blue spectra are discussed in Section 4.2.3.

is 85 d. Given its radius, the equatorial $v\sin i$ is expected to be 100–200 m s^{-1} which would be impossible to detect with HARPS.

4 RESULTS

4.1 AlH opacity

In the left-hand panel of Fig. 2, we show the computed absorption coefficient per AlH molecule

$$k_o = 0.02654 \times gf \times \exp(-E/kT)/U(T)$$

of the AlH molecule computed across different spectral ranges. We computed k_o for the case of $T = 2900$ K, it is the effective temperature of Proxima Cen, adopted here; U(2900K) = 315.9 (Yurchenko et al. 2018). The blue spectral range shown in the right-hand panel of Fig. 2 should reveal stronger lines compared to the redder region.

4.2 Identification and fit to AlH lines in Proxima Cen spectrum

Because AlH is a light molecule (i.e. has large rotational constants and spacing), its spectrum consists of a set of strong but well-separated lines providing a new tool to study the properties of stellar atmospheres.

To identify AlH lines of notable intensities in Proxima Cen spectrum, we followed a simple algorithm. The residual fluxes $r_{1\nu} = F_\nu/F_\nu^c$ were computed in the spectral range 4000– 5300 Å, where F_ν, F_ν^c are theoretical fluxes in line + continuum and pure continuum spectra, respectively. To compute F_ν, we accounted for all known molecules, including AlH. We then computed similar $r_{2\nu} = F_\nu/F_\nu^c$, but with AlH excluded from the opacity list. A comparison of the ratio $R_\mathrm{f} = r_{2\nu}/r_{1\nu}$ with the observed spectrum should identify the true AlH lines in the observed spectrum. Indeed, in the AlH-free spectral ranges we get $R_\mathrm{f} = 1$, deviation of R_s from 1.0 is possible only in the case of the presence of notable, i.e. strong, AlH lines.

Table 2. List of diffuse lines in 1-0, 0-0, and 1-1 bands of ^{27}AlH A $^1\Pi$–X $^1\Sigma^+$ system.

λ_{air}^{ExoMol}	$\lambda_{air}^{observed}$	Band (v'–v'')	Branch	J″	EXOMOLś wavenumber (cm^{-1})	log($\gamma_R^{adjusted}$)
4245.2603	4245.281	0-0	R	18	23549.051639	
4247.3930	4247.464	0-0	R	19	23537.227171	*10.5*
4250.1028	4250.314	0-0	R	20	23522.220420	*11.0*
4291.7985	4291.858	0-0	Q	20	23293.701420	10.5
4296.6041	4296.801	0-0	Q	21	23267.648835	11.0
4302.0621	4302.486	0-0	Q	22	23238.129665	11.5
4308.2692	4309.054	0-0	Q	23	23204.650335	12.2
4315.3330	4316.898	0-0	Q	24	23166.667365	12.5
4338.0872	4338.162	0-0	P	21	23045.155235	*10.5*
4344.9708	4345.160	0-0	P	22	23008.646365	*11.0*
4352.4945	4352.859	0-0	P	23	22968.874335	*11.5*
4071.1444	4071.182	1-0	R	9	24556.183970	
4073.7137	4073.816	1-0	R	10	24540.696761	
4076.9591	4077.132	1-0	R	11	24521.161959	
4096.6652	4096.765	1-0	Q	11	24403.210359	
4108.0923	4108.638	1-0	Q	13	24335.331507	
4114.9229	4114.949	1-0	P	11	24294.937159	
4121.6478	4121.753	1-0	P	12	24255.297868	
4129.0516	4129.282	1-0	P	13	24211.806907	
4356.5365	4356.568	1-1	R	9	22947.564144	
4358.7835	4358.895	1-1	R	10	22935.734570	
4384.3032	4384.410	1-1	Q	11	22802.234926	
4389.5647	4389.828	1-1	Q	12	22774.903754	
4395.6399	4395.926	1-1	Q	13	22743.427113	

4.2.1 Lines formed from the rotational levels of low J

Fig. 1 shows the dependence of R_f versus wavelength computed over a wide spectral range together with the reduced pseudo-continuum observed in the Proxima Cen spectrum (see Section 2). A lot of strong AlH lines manifest themselves in the Proxima Cen spectrum. Unfortunately, we can perform such an analysis only at the wavelengths 4000–4400 Å where TiO and other molecules provide comparatively weak absorption, see the left-hand panel of Fig. 1.

We find more than 120 AlH lines formed from the rotational level of low J can be clearly identified in the spectrum of Proxima Cen and were therefore important to include in our model.

The agreement between the simulation and the observed spectrum is quite good over wide spectral ranges confirming the high accuracy of the ExoMol line list in their wavelengths and intensities at least for lines of lower J; however, see the next section.

Only a few AlH lines in the selected spectral ranges could not be matched to the theoretical data, all corresponding to higher J, i.e. R(10), R(11), and R(19-22), on the left- and right-hand panels of Fig. 3, respectively. A list of AlH lines which were found to coincide in the theoretical and observed spectra are collected in Table A1. We restrict our analysis to wavelengths $\lambda < 4400$ Å, as at the longer wavelengths AlH lines are severely blended with features due to TiO and other molecules, see Fig. 1.

The ExoMol lines which are absent or misplaced (see, however, the next subsection) in the observed Proxima Cen spectrum are listed in the Table A2. As we noted above, they are formed by transitions between upper rotational levels for which spectroscopic parameters were obtained by extrapolation from the lower levels data, see Yurchenko et al. (2018). These lines are marked by open triangles in Fig. 3.

4.2.2 AlH transitions with higher J *– diffuse lines*

AlH lines with values of $J > 18$ in the 0-0 band and $J > 10$ in the 1-0 and 1-1 bands presented in Table 2 are described as HJ (high J) lines below. The majority of the AlH lines corresponding to remaining lines are remarkably well reproduced by the ExoMol list of lines. Still, some distinct deviations were found for higher J lines in the 0-0, 1-0, and 1-1 bands of the A $^1\Pi$ –X $^1\Sigma^+$ system exhibiting the following regular patterns of behaviour:

(i) HJ line positions are systematically redshifted relative to the calculated wavelengths with the intervals increasing with J;
(ii) The shifts in HJ line positions are accompanied by the systematic increase in their linewidths.

These findings are illustrated in Figs 4 and 5.

Fig. 4 shows the spectrum of Proxima Cen in three selected spectral ranges of the 0-0 A $^1\Pi$ – X $^1\Sigma^+$ band of ^{27}AlH. The three panels show systematic changes in observed profiles of the high-J members of R (top panel), Q (middle panel), and P (bottom panel) branches. The ExoMol line positions are marked with solid lines. The lines showing difference in position with the calculated values is colored in red. The observed line positions are shown with the red dashed vertical lines. The higher members of the series, up to $J' = 25$, are either blended by strong and wide atomic lines [see R(21) on the top panel of Fig. 4], contaminated by the instrumental effects [R(22), P(24)], or are below the confusion limit [R(23), R(24), P(25), P(26)]. In summary, none of the analysed lines is inconsistent with the observed spectrum, if wavelength corrections are taken into account. The first observable signature of varying line position in the 0-0 band begins around $J' = 19$ [R(18)].

Fig. 5 shows the spectrum of Proxima Cen in four selected spectral ranges covering the 1-0 and 1-1 bands. The two upper panels show systematic changes in observed profiles of the members of the R-

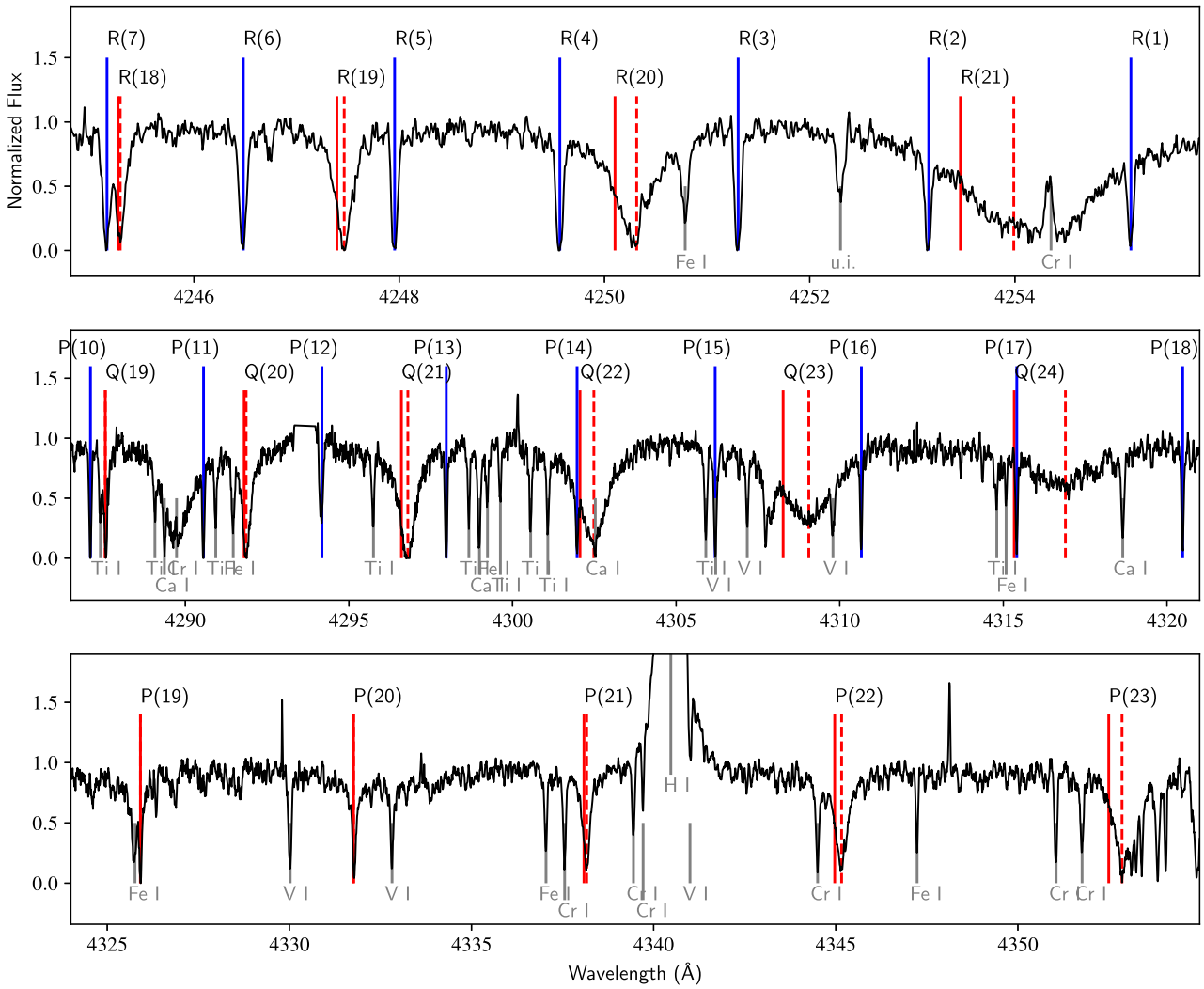

Figure 4. Spectrum of Proxima Cen in the spectral range covering selected intervals of the ^{27}AlH A $^1\Pi$ – X $^1\Sigma^+$ 0-0 band. The lines of diffuse nature are marked in red. The vertical lines mark calculated positions of lines, while the dashed ones mark the observed positions; the R(21) in the top panel is heavily blended by the CrI resonance line and not marked. Atomic lines are marked in grey.

branch (top panel), and Q and P-branches (the panel in the second row) of the 1-0 band. The two bottom panels illustrate the same for members of the R-branch (the third row), and P- and Q-branches (the bottom panel) of the 1-1 band. The colour scheme is the same as in Fig. 4. The transitions of 1-0 and 1-1 bands share the same upper rotational states of the $v' = 1$. The observable departure from line positions begin at J' of 10 (R(9)). The highest J' transitions may be traced up to $J' = 13$ [1-0 Q(13) at 4108 Å and 1-1 Q(13) at 4396 Å]. The two lines of 1-0 Q(14) and Q(15) are expected to be shallow and could vanish in the continuum tracing process.

There are a number of atomic lines in the range of spectrum covering 1-0, 0-0, and 1-1 bands of A-X system. Some of these lines are intense enough to be saturated and develop Lorentz wings, e.g. the Fe I multiplet; one member at 4071.8 Å contaminates the wings of the already diffuse 1-0 R(9) line. The weaker one has intensities and shapes comparable to those of molecular lines. Hence, care must be taken to estimate their contribution in case of blending with molecular lines. Unfortunately, the spectral synthesis does not always help, as modeling the spectrum of M dwarf in the near UV range has some drawbacks mentioned below (Section 4.2.3). In cases of such problematic overlapping with atomic lines we compare the line intensity with other members of the same multiplet, or neighbouring multiplets. Possible contaminations include the 0-0 diffuse R(21) line overlaps with very strong Cr I (4254.2 Å) disabling any conclusions. To compare other member of the same Cr I, multiplet is observed at 4289.9 Å. The diffuse Q(22) line is contaminated by Ca I, but here the strength of other member of the multiplet, Ca I at 4318 Å is low enough to show that the atomic line can be neglected. The diffuse P(23) line is contaminated by V I at 4352.8 Å. The 1-0 diffuse Q(12) line overlaps with the Hδ line completely erasing the presence of absorption. Note, that the molecular line may influence the shape of the hydrogen emission line.

The list of lines of the 0-0, 1-0, and 1-1 bands for which we observe departure from the ExoMol line positions is presented in Table 2. The first column contains the original line wavelengths calculated from the energies of the upper and lower states, in cm^{-1}, and converted to air (Ciddor 1996). The second column contains line positions measured in the spectrum. The uncertainty of line measurement is estimated as 0.05 Å. The third, fifth, and sixth columns contain identification of transitions: vibrational numbers of the upper and lower states, branch and the rotational quantum numbers of the lower level, respectively. The seventh column contains the transition

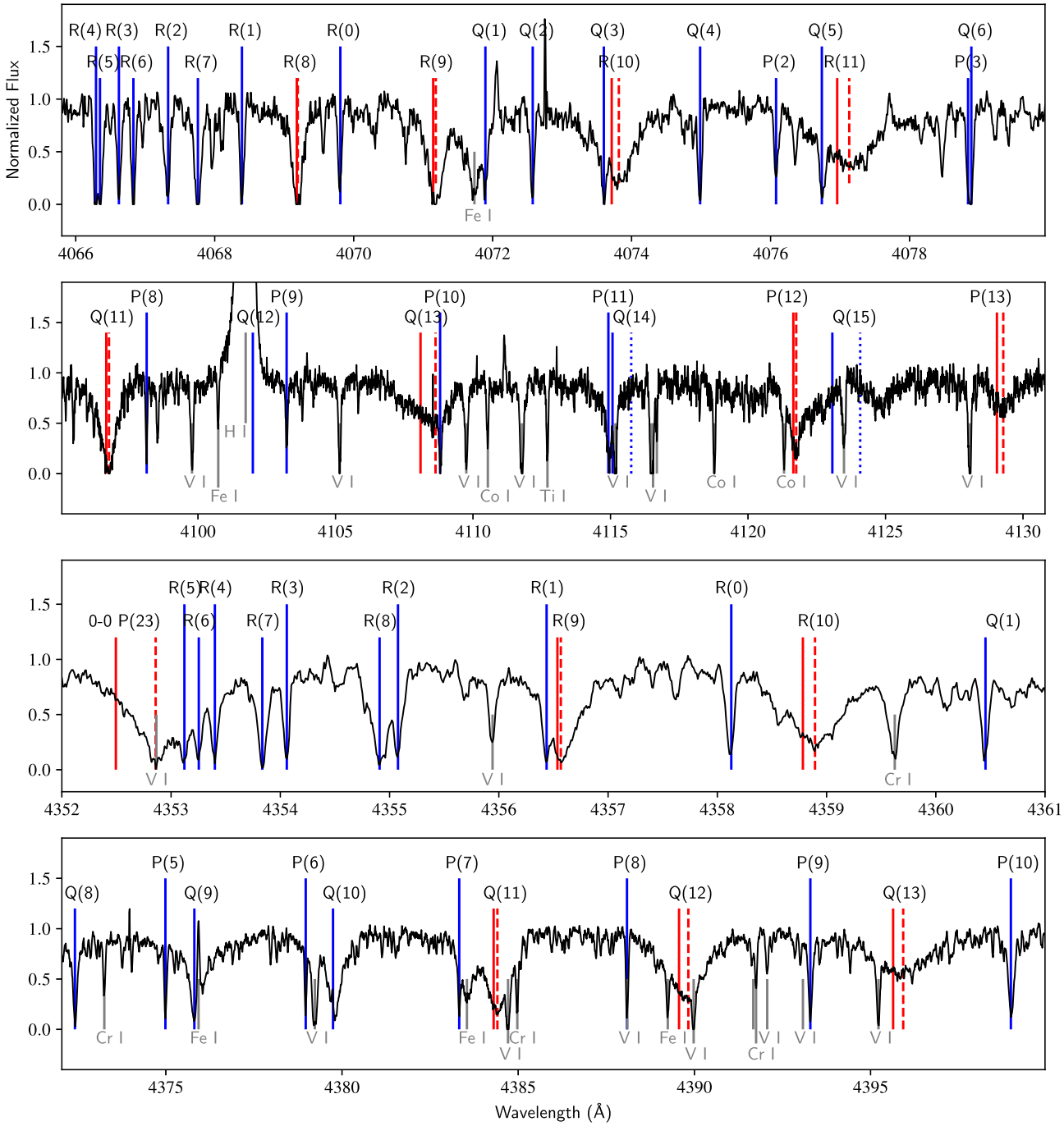

Figure 5. Spectrum of Proxima Cen in the spectral range covering selected parts of the ^{27}AlH A $^1\Pi$ – X $^1\Sigma^+$ 1-0 (upper two panels) and 1-1 (the lower two panels) bands. The lines of diffuse nature are colored in red. The vertical lines mark calculated positions of lines, while the dashed ones mark the observed positions. Extrapolated and very uncertain positions of 1-0 Q(14) and Q(15) lines at the second panel from the top are marked with dotted lines. Atomic lines are marked in grey. The transition P(23) at 4352.8 Å (the third row) belongs to the 0-0 band.

wavenumber. The last column contains empirical damping rates as described in the next subsection. The values of damping rates in italic are adopted from the empirical damping rates of the Q-branch.

Assuming that the differences between the calculated and observed wavelengths are mainly due to the inaccurate energies of the upper states one can observe how energies change with the rotational number. This is presented in Fig. 6. Note the negative sign of the shift which means that the observed upper states should have lower energy than the calculated ones. A third-order polynomial fit is used as the guiding line. Here, we assume that the splittings of the *e* and *f* components (in expanded notation Q and R are in fact Q_{11fe} and R_{11ee}) of the A $^1\Pi$ state are unaffected by the observed differences.

4.2.3 *Fit to the HJ lines broadened*

We carried out a few numerical experiments to consider in detail the fits of our model spectra to some diffuse AlH lines of the Q

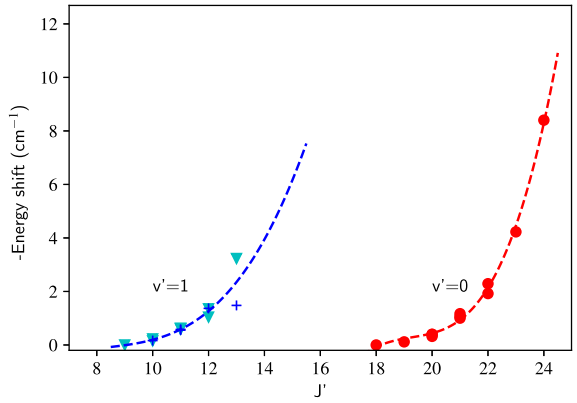

Figure 6. Absolute correction to the energy of the rotational levels of the A $^1\Pi$ $v = 1$ and $v = 0$ states necessary to reproduce observed wavelengths. Note that the sign of the correction is negative. For the v'=1 upper state, the points correspond to the transitions of the 1–0 and 1–1 bands. For the v′ = 1 upper state, the points correspond to the transitions of the 1–0 (cyan triangles) and 1–1 bands (blue crosses).

(0-0) branch in the observed spectrum of Proxima Cen, see Fig. 7. Pavlenko et al. (2017) showed that some theoretically computed atomic lines in the blue spectrum of Proxima Cen are too strong compared to the observations. We see the same in the top panel of Fig. 7. To reduce their strengths, we followed the procedure proposed by Pavlenko et al. (2017). Namely, we computed synthetic spectra with the account of an additional continuum opacity, i.e. we adopted

$$k_\nu^c = k_\nu^{c\times} \times K_x, \tag{7}$$

where $k_\nu^{c\times}$ is the conventional continuum opacity and K_x is an adjusting parameter. The discussion of the 'missing opacity' problem is beyond the scope of this paper, see Pavlenko et al. (2017). Nevertheless, the implementation of K_x allowed us to improve the fits to observed profiles of strong absorption lines of atoms, see the top panel of Fig. 7.

The adopted parameter K_x also affects the broad molecular HJ lines. To fit the HJ lines, we followed the procedure:

(1) We used the observed wavelengths of AlH lines in Proxima Cen spectrum for the transitions Q(21), Q(22), Q(23), and Q(24) of the 0-0 band. The shifts of some AlH lines are shown in Fig. 7 and Table 2.

(2) Predissociation effects of AlH are known to be responsible for the increased broadening of the lines. To fit the computed profiles to the observed lines in spectra of Proxima Cen, we adjusted the parameters of the Lorenz profile $\gamma_R^{\rm adjusted} = a_x \times \gamma_R$, where a_x varies from a few hundreds to 10^5. The optimal values of log γ_R found are shown in Table 2, too. It is worth noting that both $\gamma_R^{\rm adjusted}$ and the widths of the HJ lines depend on J.

Interestingly, the broadening effect of the strong HJ lines removes their saturation and thus provides the opportunity to use them for the Al abundance determination. Indeed, the broadening line width of the predissociative AlH lines does not depend on the external factors, such as temperature, pressure, etc., $\gamma_R^{\rm adjusted}$ is only a function of J for the given transition. In fitting to the line width we took into account also thermal broadening and Van der Waals broadening through its classical formula. While saturated lines of lower J show rather marginal changes, the non-saturated, broadened HJ lines show a significant dependence on the adopted Al abundance, see the middle panel of Fig. 7. This makes them a useful abundance diagnostic. We can get the proper fit to the strong (saturated) and diffuse (non-saturated) lines in the the framework of one model.

Conversely, fits to the observed spectra reveal the degeneracy of the solution in the sense that we cannot determine the abundance of aluminum only from fitting of the AlH line profiles. For example, our fits are shown in Fig. 7 provide [Al/Fe] $= -1.0, -0.3$, and -0.1 with approximately the same quality of the fit for the cases $K_x = 1.0, 40.0, 80.0$, respectively. Interestingly, these results were obtained for the same AlH line list with these adjusted wavelengths and broadening parameters.

However, we know that abundances in the Proxima Cen atmosphere is near solar, see Pavlenko et al. (2017), and references therein, which provides an additional restriction on the model atmosphere parameters. Two other components of α Cen triple system shows rather weak metal overabundance, see Introduction. Therefore, when we use the unsaturated diffuse AlH lines which are sensitive to aluminium abundance, we can exclude solution with $K_x = 1$, and we get [Al] $= -0.1$: -0.3 for Proxima Cen.

4.3 Discussion of lifetimes of predissociated levels of AlH

In the previous section, we estimated the radiative damping rates necessary to explain line shapes of selected HJ transitions (see Table 2). The damping rates increase systematically with the rotational number J. The explanation of the effect was discussed in Baltayan & Nedelec (1979) and shortly described in the introduction. Baltayan & Nedelec (1979) used literature spectra of AlH (Bengtsson & Rydberg 1930; Hulthén & Rydberg 1933) to extract information on the linewidths of selected transitions. Below, we used the same approach to our estimations of linewidths.

Here, we assume that the damping rates of the HJ AlH lines are dominated by the dissociative lifetime of the upper predissociated level. In Table 3, we compare empirically determined values in this paper with the literature estimations of dissociative lifetimes Baltayan & Nedelec (1979) (see their table III). The formal accuracy of τ determination is based on the uncertainty of the fit of radiative damping rates, see Fig. A1 as well.

4.4 Comparison of ExoMol and REALH

Fig. 8 compares ExoMol and REALH simulations with the observed Proxima Cen spectra. In our computations we increase *gf* of REALH by a factor of 10 to get better agreement with ExoMol. All spectra were computed with the same input parameter sets besides the AlH line lists. We find that ExoMol provides better agreement with the line positions observed in the Proxima spectrum. ExoMol also provides a better description of lines with a doublet structure in comparison to REALH, see detail at 4245.325 Å in the middle panel of Fig. 8.

4.5 Searching for ^{26}Al^{1}H lines in Proxima Cen spectrum

The long history of observations of Proxima Cen provides a lot of evidence about the comparatively high level of activity observed in Proxima Cen (see Introduction). It is possible that mighty stellar flares may generate cosmic rays with the high energy needed to create observable amounts of radioactive ^{26}AlH. This possibility can be tested by direct comparison of the computed ^{26}Al^{1}H spectrum with observations. The spectroscopic line list for the ^{26}AlH molecule was computed by ExoMol using the same spectroscopic model as for ^{27}AlH and we expect the similar quality of line position determination for the transitions between levels of low J, even without the 'MARVELIsation' procedure used for ^{27}AlH. However,

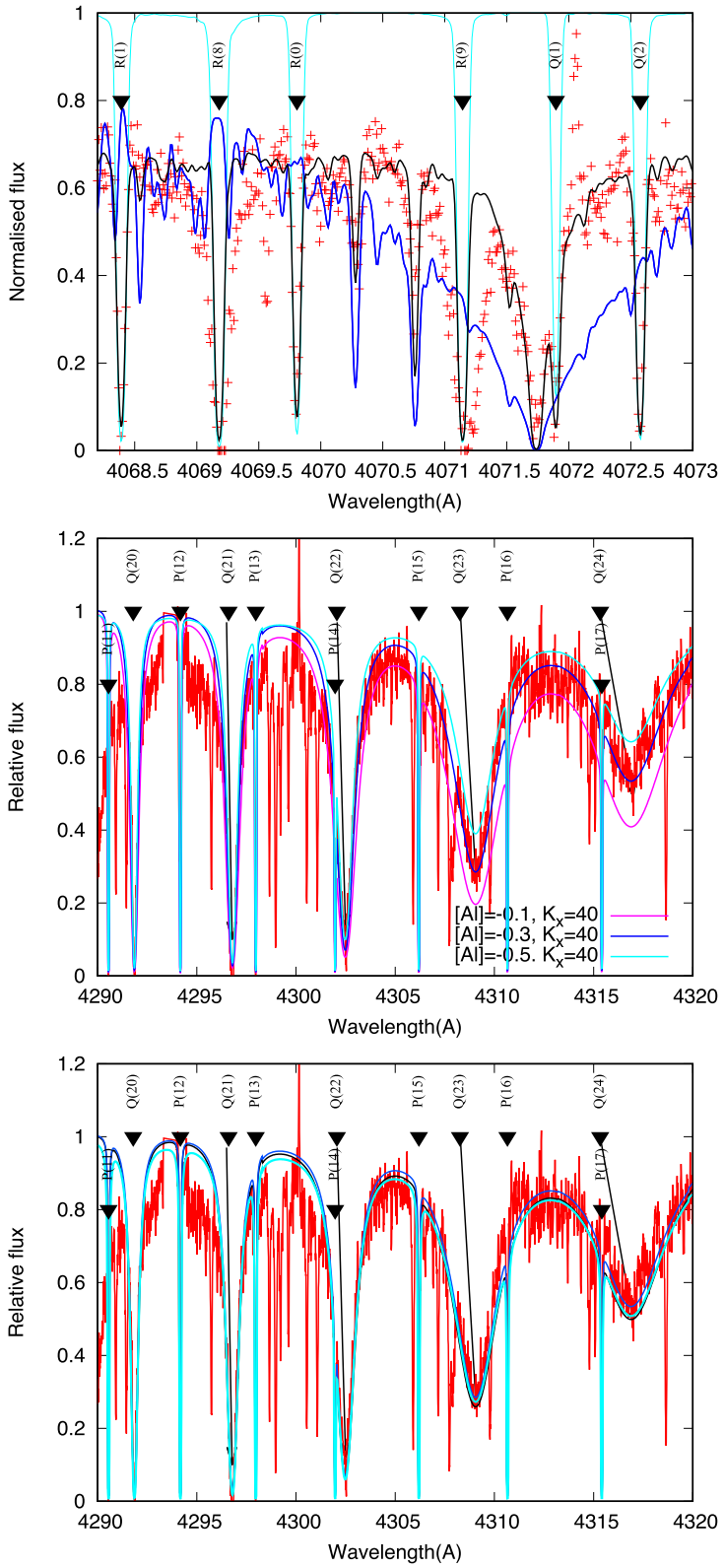

Figure 7. Top panel: Panel illustrating fitting of strong atomic absorption lines in the observed spectrum. Blue line shows spectrum computed without AlH lines with $K_x = 1$, black line shows the 'AlH on' case with $K_x = 40$. The broad absorption feature at 4071.738 Å is due to the Fe I line. The cyan line shows contribution of AlH lines R_f. Middle panel: Dependence of saturated and unsaturated HJ lines on Al abundance. Bottom panel: Fit to broadened HJ lines of AlH with parameters shown in Table A3 to the observed Proxima Cen spectrum. Three cases of the fit are shown: $K_x = 1$ (cyan line) provides [Al/Fe] $= -1.0$, blue line shows $K_x = 40$, [Al/Fe] $= -0.3$, and black line shows $K_x = 80$, [Al/Fe] $= -0.1$. Arrows show the 'true' positions of some AlH lines from the Q branch of (1-0) band. The damping parameters are always the same, see Table A3.

Table 3. Dissociative lifetimes of AlH in the $v' = 0$ state measured from linewidths by Baltayan & Nedelec (1979) (Lab) and derived from damping rates in this work.

J'	Lab τ (10^{-13} s)	our τ (10^{-13} s)
21	99	100(+ 100)(−50)
23	9.2	6.3(+ 2.6)(−1.8)
24	4.5	3.2 ± 0.7

our comparison of theoretical and observed spectra does not reveal any noticeable features at the wavelengths of ^{26}Al^{1}H lines, instead of just the ^{27}Al^{1}H lines which all can be identified at the predicted locations, see Fig. 9. Fits to the observed AlH lines shown allow us to determine an upper level of the isotopic ratio ^{27}Al /^{26}Al > 99 (Fig. 9). Thus, ^{26}Al is not present in the atmosphere of Proxima Cen in noticeable amounts. Strictly speaking, this result does not seem to be surprising. Indeed, we can expect that even a large quantity of ^{26}Al is formed in a mighty stellar flare should be diluted on a short time scale by the strong convective envelope that extends to the core.

5 CONCLUSIONS

Our work confirms the presence of many AlH lines in the spectrum of Proxima Cen (M5.5 V). These identifications are confirmed by direct comparison of computed and observed spectra of the star in the blue spectral range. Indeed, AlH lines at the predicted wavelengths appear in the theoretical spectrum only when the AlH line is included in the opacity list. In some spectral ranges, e.g. 4065–4090 and 4240–4280 Å they dominate in number and intensity over other molecular features. Because AlH is classified as a 'light' molecule, the AlH spectrum of Proxima Cen consists of a set of strong but well-separated lines, even across the molecular band heads.

Our comparison with the observed spectrum of Proxima Cen confirms the high accuracy of the ExoMol line list, in terms of the match in wavelength and intensity at least for the case of transitions between levels of lower rotational excitation energy. The structure of the molecular bands of AlH bands agrees well with observations across a considerable spectral range. They have a well-defined structure consisting of single lines that do not form blends in the high resolution spectra. In other words, the AlH bands are made up of well-separated lines that provide a one-of-a-kind tool for studying the properties of stellar atmospheres. We believe the best targets for the realization of these ideas would be M-dwarfs of earlier spectral classes showing less blended spectra, or even subdwarfs with a slight deficit of Al.

Along with this, we identified some broad lines in the observed spectrum of Proxima Cen as AlH lines formed by transitions between higher J levels. These lines are shifted with respect to the ExoMol predicted wavelengths and we compute the energy corrections for the rotational levels of the $A\,^1\Pi$ $v = 1$ and $v = 0$ states required to reproduce observed wavelengths. These lines are substantially broadened due to the large widths of predissociation levels. We fitted to them by adjusting the values of γ_R.

Empirical radiative damping of lines gives direct information on lifetime of the upper rotational states. We found that our values agree almost perfectly with those obtained by Baltayan & Nedelec (1979).

Our work shows that real stellar spectra of high quality provides an excellent tool for verifying the output of complicated quantum-mechanical procedures and may serve as a source of data extending that available in the laboratory. Not only of line positions but also of information on the lines broadening. In particular, empirical determination of radiative damping rates for a larger number of AlH lines from modeling of stellar spectra would be very beneficial, especially for lines inaccessible in the spectrum presented here. To this end, even not very-high resolution spectra covering a spectral range of order of hundred Å but with a well-defined flat continuum and with high signal-to-noise ratio would be very useful.

The original model used to construct the WYLLoT line lists neglected the possibility of predissociation. Recent theoretical developments (Pezzella, Yurchenko & Tennyson 2021) allow for the continuum and predissocation effects to be properly included in the spectroscopic model solved by Duo. For AlH, these effects should help model the line broadening of the predissociated states and will be the subject of future study. However, ExoMol line lists rely heavily on the availability of laboratory high-resolution spectra to obtain reliable line positions, intensities and line shapes. Therefore, further AlH laboratory work would undoubtedly help here.

It is worth noting that the $A\,^1\Pi$–$X\,^1\Sigma^+$ system of AlH with its low J predissociation limit in its upper $v' = 0$ and 1 states represents itself a rare example of molecular bands for which the list of molecular lines updated with radiative damping information may be 'astrophysically complete'. Very similar work presenting extended list of lines of ^{12}CH and ^{13}CH based partly on the analysis of stellar spectrum of the carbon-enhanced metal-poor objects was performed by Masseron et al. (2014). We believe, that our study shows the importance of using lines of the AlH molecule as a powerful tool in astrophysical investigations of the atmospheres of late-type stars.

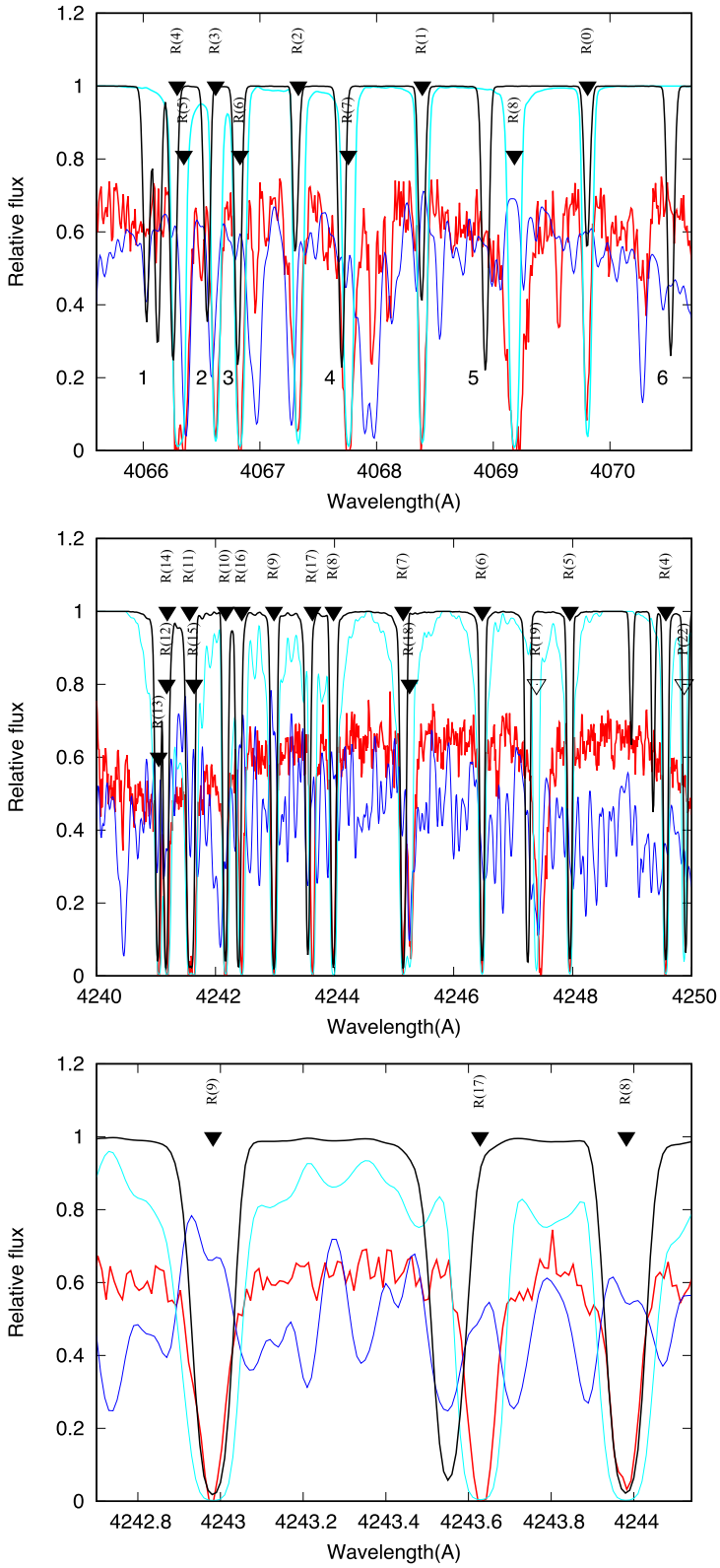

Figure 8. Fit of our model spectra computed with ExoMol (cyan line) and REALH (black line) lists to the two selected spectral ranges. Red and blue lines show the observed, and computed spectrum without AlH lines spectra, respectively. In the top panel we mark the spectral details which differ for two cases, by numbers: 1 denotes different structure of the band heads, 2, 3, 4 shows a notable shifts of REALH AlH lines with respect to the observed and ExoMol lines, 4, and 5, 6 mark misplaced REALH lines. The middle and bottom panel show a similar picture for (1,1) band head. The bottom plot shows a portion of the middle plot on an expanded scale.

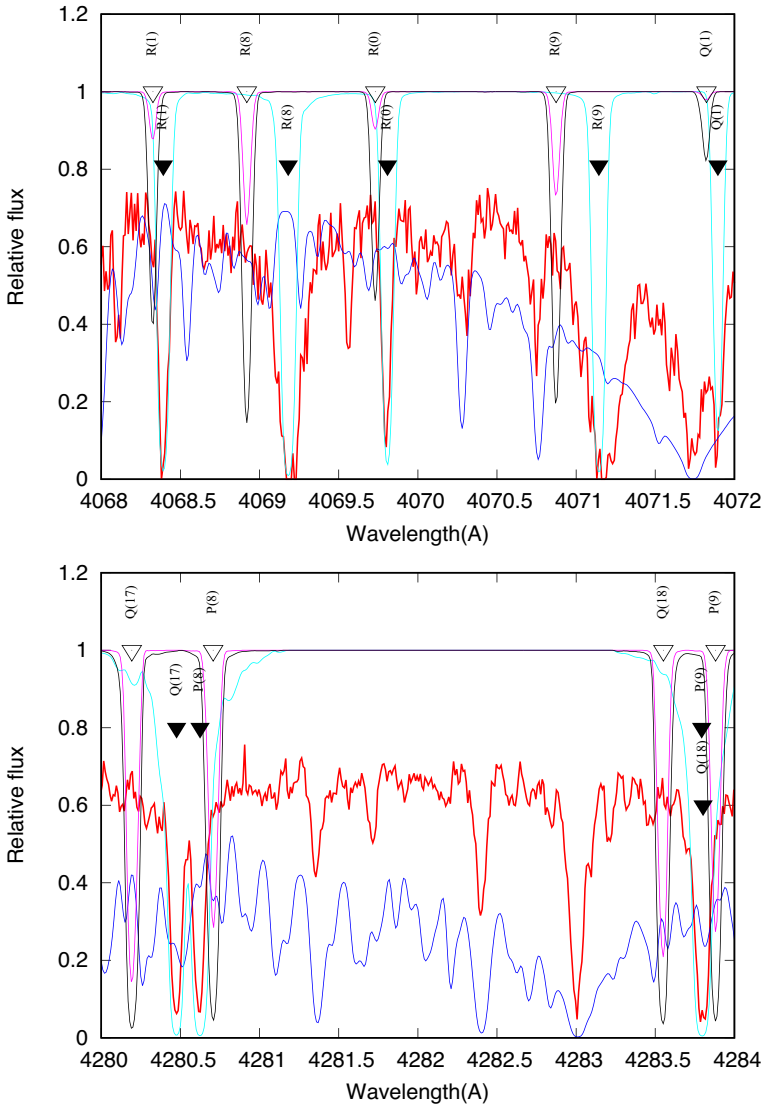

Figure 9. Comparison of the computed R_f for ^{26}Al^{1}H and ^{27}Al^{1}H shown by black and cyan lines, respectively, with two arbitrary selected spectral ranges of the Proxima Cen spectrum shown by red line. The pink line shows R_f computed for the case of reduced by two orders abundance of ^{26}Al. The blue line shows the theoretical spectrum without AlH lines. Central wavelengths of theoretical lines of ^{26}Al^{1}H and ^{27}Al^{1}H are marked by ▽ and ▼, respectively. We depict the spectroscopic identification of these lines, as well.

ACKNOWLEDGEMENTS

This study was funded as part of the routine financing programme for institutes of the National Academy of Sciences of Ukraine. This research is based on observations collected at the European Organisation for Astronomical Research in the Southern Hemisphere under ESO programme(s) 087.D-0300(A). This research has made use of the services of the ESO Science Archive Facility. The ExoMol project is funded by the European Research Council (ERC) under the European Union's Horizon 2020 research and innovation programme through Advance Grant number 883830 and STFC through grant ST/R000476/1. YP acknowledges financial support from the Agencia Estatal de Investigación of the Ministerio de Ciencia, Innovación y Universidades through the Centre of Excellence 'Severo Ochoa' award to the Instituto de Astrofísica de Canarias (CEX2019-000920-S)', while this work was being completed. MRS and YVP acknowledge funding from grant no 2018/30/E/ST9/00398 from the Polish National Science Center. HRAJ acknowledges support from STFC award ST/T007311/1. This research has made use of the VALD database, operated at Uppsala University, and of NASA's Astrophysics Data System Bibliographic Services (ADS). We thank R.L. Kurucz for his great work on creating the data for all the line lists. We thank the anonymous referee for a thorough review and we highly appreciate the comments and suggestions, which significantly contributed to improving the quality of the paper.

DATA AVAILABILITY

The data used in this paper are available in the various archives and databases as follows:

ESO HARPS archive: http://archive.eso.org/wdb/wdb/adp/phase3_main/query

ExoMol database: https://www.exomol.com/

Kurucz molecular list database: http://kurucz.harvard.edu/molecules.html

VALD database: http://vald.astro.uu.se/

REFERENCES

Allard F., 2014, in Booth M., Matthews B. C., Graham J. R., eds, IAU Symp. Vol. 299, Exploring the Formation and Evolution of Planetary Systems. Kluwer, Dordrecht, p. 271

Anders E., Grevesse N., 1989, Geochim. Cosmochim. Acta, 53, 197

Araujo-Escalona V. et al., 2015, AIP Conference Proceedings, 1671, 030003

Araujo-Escalona V. et al., 2016, J. Phys. Conf. Ser., 730, 012003

Baltayan P., Nedelec O., 1979, J. Chem. Phys, 70, 2399

Bengtsson E., Rydberg R., 1930, Zeitschrift fur Physik, 59, 540

Bessell M. S., 2011, in Johns-Krull C., Browning M. K., West A. A., eds, ASP Conf. Ser. Vol. 448, 16th Cambridge Workshop on Cool Stars, Stellar Systems, and the Sun. Astron. Soc. Pac., San Francisco, p, 131

Burrows A., Volobuyev M., 2003, ApJ, 583, 985

Casali G. et al., 2020, A&A, 639, A127

Cernicharo J., Guelin M., 1987, A&A, 183, L10

Ciddor P. E., 1996, Appl. Opt., 35, 1566

Cretignier M., Francfort J., Dumusque X., Allart R., Pepe F., 2020, A&A, 640, A42

Farkas L., 1931, Zeitschrift fur Physik, 70, 733

Furtenbacher T., Császár A. G., Tennyson J., 2007, J. Mol. Spectrosc., 245, 115

Gurvich L. V., Veits I. V., Alcock C. B., 1989, Thermodynamics properties of individual substances. Volume 1 - Elements O, H/D, T/, F, Cl, Br, I, He, Ne, Ar, Kr, Xe, Rn, S, N, P, and their compounds. Part 1 - Methods and computation. Part 2 - Tables (4th revised and enlarged edition). Hemisphere Publishing Corp., New York, p. Pt. 1, 577

Halfen D. T., Ziurys L. M., 2014, ApJ, 791, 65

Herbig G. H., 1956, Publ. Astron. Soc. Pac., 68, 204

Howard W. S. et al., 2018, ApJ, 860, L30

Hulthén E., Rydberg R., 1933, Nature, 131, 470

Ito F., Nakanaga T., Takeo H., Jones H., 1994, J Mol. Spectrosc, 164, 379

Johnson H. R., Sauval A. J., 1982, A&AS, 49, 77

Kamiński T., Schmidt M. R., Menten K. M., 2013, A&A, 549, A6

Kamiński T. et al., 2016, A&A, 592, A42

Kamiński T. et al., 2018, Nat. Astron., 2, 778

Karthikeyan B., Rajamanickam N., Bagare S. P., 2010, Sol. Phys., 264, 279

Kurucz R. L., 1970, Atlas: A Computer Program for Calculating Model Stellar Atmospheres. Smithsonian Astrophysical Observatory, CFA Harward

Kurucz R. L., 2011, Can. J Phys, 89, 417

Kurucz R., 2014, Model Atmosphere Codes: ATLAS12 and ATLAS9. Springer International Publishing (Cham), p. 39

Lodders K., Palme H., Gail H. P., 2009, Landolt Börnstein, 4B, 712

MacGregor M. A. et al., 2021, ApJ, 911, L25

Masseron T. et al., 2014, A&A, 571, A47

Mayor M. et al., 2003, The Messenger, 114, 20

McKemmish L. K., Masseron T., Hoeijmakers H. J., Pérez-Mesa V., Grimm S. L., Yurchenko S. N., Tennyson J., 2019, MNRAS, 488, 2836

Palmerini S. et al., 2020, Proceedings of the 15th International Symposium on Origin of Matter and Evolution of Galaxies (OMEG15)

Pavlenko Y. V., 1997, Ap&SS, 253, 43

Pavlenko Y. V., 2014, Astron Rep., 58, 825

Pavlenko Y., Zapatero Osorio M. R., Rebolo R., 2000, A&A, 355, 245

Pavlenko Y., Suárez Mascareño A., Rebolo R., Lodieu N., Béjar V. J. S., González Hernández J. I., 2017, A&A, 606, A49

Pavlenko Y. V., Suárez Mascareño A., Zapatero Osorio M. R., Rebolo R., Lodieu N., Béjar V. J. S., González Hernández J. I., Mohorian M., 2019, A&A, 626, A111

Pavlenko Y. V., Yurchenko S. N., Tennyson J., 2020, A&A, 633, A52

Pezzella M., Yurchenko S. N., Tennyson J., 2021, Phys. Chem. Chem. Phys., 23, 16390

Qin Z., Bai T., Liu L., 2021, ApJ, 917, 87

Ram R. S., Bernath P. F., 1996, Appl. Opt., 35, 2879

Ryabchikova T., Pakhomov Y., 2015, Baltic Astron, 24, 453

Sauval A. J., Tatum J. B., 1984, ApJS, 56, 193

Sitnova T. et al., 2015, ApJ, 808, 148

Steinmetz M. et al., 2020, AJ, 160, 83

Szajna W., Zachwieja M., 2009, European Phys. J D, 55, 549

Tenenbaum E. D., Ziurys L. M., 2010, ApJ, 712, L93

Tennyson J. et al., 2020, J. Quant. Spectrosc. Radiat. Transf., 255, 107228

Tsuji T., 1973, A&A, 23, 411

Unsold A., 1955, Physik der Sternatmospharen, MIT besonderer Berucksichtigung der Sonne. Springer, Berlin

Wallace L., Hinkle K., Livingston W., 2000, An atlas of sunspot umbral spectra in the visible, from 15,000 to 25,500 cm(-1) (3920 to 6664 [Angstrom]). National Optical Astronomy Observatories, Tucson, Ariz.

White J. B., Dulick M., Bernath P. F., 1993, J. Chem. Phys., 99, 8371

Yurchenko S. N., Lodi L., Tennyson J., Stolyarov A. V., 2016, Comput. Phys. Commun., 202, 262

Yurchenko S. N., Williams H., Leyland P. C., Lodi L., Tennyson J., 2018, MNRAS, 479, 1401

Zhu Y. F., Shehadeh R., Grant E. R., 1992, J. Chem. Phys., 97, 883

Ziurys L. M., Savage C., Highberger J. L., Apponi A. J., Guélin M., Cernicharo J., 2002, ApJ, 564, L45

APPENDIX A: EXTRA MATERIAL

Table A1. ExoMol AlH lines present in both theoretical and observed spectra of Proxima Cen.

Wavelength in air (Å)	Branch(j)	v'	v''
4066.292	R(4)	1	0
4066.349	R(5)	1	0
4066.621	R(3)	1	0
4066.830	R(6)	1	0
4067.330	R(2)	1	0
4067.758	R(7)	1	0
4068.392	R(1)	1	0
4069.181	R(8)	1	0
4069.808	R(0)	1	0
4071.144	R(9)	1	0
4071.896	Q(1)	1	0
4072.577	Q(2)	1	0
4073.601	Q(3)	1	0
4074.986	Q(4)	1	0
4076.079	P(2)	1	0
4076.738	Q(5)	1	0
4078.842	P(3)	1	0
4078.890	Q(6)	1	0
4081.452	Q(7)	1	0
4081.957	P(4)	1	0
4084.467	Q(8)	1	0
4085.423	P(5)	1	0
4087.971	Q(9)	1	0
4089.265	P(6)	1	0
4093.490	P(7)	1	0
4098.135	P(8)	1	0
4101.994	Q(12)	1	0
4103.223	P(9)	1	0
4108.804	P(10)	1	0
4117.173	R(17)	1	0
4184.831	Q(20)	1	0
4229.014	P(21)	1	0
4241.046	R(13)	0	0
4241.179	R(12)	0	0
4241.189	R(14)	0	0
4241.562	R(11)	0	0
4241.641	R(15)	0	0
4242.169	R(10)	0	0
4242.440	R(16)	0	0
4242.982	R(9)	0	0
4243.628	R(17)	0	0
4243.982	R(8)	0	0
4245.153	R(7)	0	0
4245.260	R(18)	0	0
4246.481	R(6)	0	0
4247.955	R(5)	0	0
4249.565	R(4)	0	0
4251.303	R(3)	0	0
4253.160	R(2)	0	0
4255.130	R(1)	0	0
4257.211	R(0)	0	0
4259.499	Q(1)	0	0
4259.708	Q(2)	0	0
4260.022	Q(3)	0	0
4260.448	Q(4)	0	0
4260.989	Q(5)	0	0
4261.652	Q(6)	0	0
4262.444	Q(7)	0	0
4263.374	Q(8)	0	0
4264.073	P(2)	0	0
4264.452	Q(9)	0	0
4265.693	Q(10)	0	0
4266.563	P(3)	0	0
4267.108	Q(11)	0	0

Table A1 – *continued*

Wavelength in air (Å)	Branch(j)	v'	v''
4268.595	R(24)	0	0
4268.716	Q(12)	0	0
4269.157	P(4)	0	0
4270.537	Q(13)	0	0
4271.856	P(5)	0	0
4272.595	Q(14)	0	0
4273.710	P(23)	1	0
4274.663	P(6)	0	0
4274.915	Q(15)	0	0
4277.532	Q(16)	0	0
4277.584	P(7)	0	0
4280.476	Q(17)	0	0
4280.624	P(8)	0	0
4283.793	P(9)	0	0
4283.802	Q(18)	0	0
4287.100	P(10)	0	0
4287.553	Q(19)	0	0
4290.556	P(11)	0	0
4291.798	Q(20)	0	0
4294.175	P(12)	0	0
4296.604	Q(21)	0	0
4297.975	P(13)	0	0
4301.973	P(14)	0	0
4306.193	P(15)	0	0
4310.662	P(16)	0	0
4315.412	P(17)	0	0
4320.481	P(18)	0	0
4325.911	P(19)	0	0
4331.761	P(20)	0	0
4353.122	R(5)	1	1
4353.254	R(6)	1	1
4353.401	R(4)	1	1
4353.835	R(7)	1	1
4354.059	R(3)	1	1
4354.909	R(8)	1	1
4355.077	R(2)	1	1
4356.437	R(1)	1	1
4358.128	R(0)	1	1
4360.455	Q(1)	1	1
4361.094	Q(2)	1	1
4361.740	R(11)	1	1
4363.368	Q(4)	1	1
4365.030	Q(5)	1	1
4365.110	P(2)	1	1
4367.075	Q(6)	1	1
4368.072	P(3)	1	1
4369.527	Q(7)	1	1
4371.361	P(4)	1	1
4372.421	Q(8)	1	1
4374.989	P(5)	1	1
4375.810	Q(9)	1	1
4375.981	R(14)	1	1
4378.971	P(6)	1	1
4383.327	P(7)	1	1
4388.087	P(8)	1	1
4393.291	P(9)	1	1
4398.981	P(10)	1	1
4430.946	Q(17)	1	1
4443.507	Q(18)	1	1
4445.583	R(20)	1	1
4475.030	Q(20)	1	1
4494.740	Q(21)	1	1
4517.686	Q(22)	1	1
4546.441	R(16)	0	1
4546.543	R(17)	0	1

Table A1 – *continued*

Wavelength in air (Å)	Branch(j)	v'	v''
4546.718	R(15)	0	1
4547.316	R(14)	0	1
4548.202	R(13)	0	1
4549.328	R(12)	0	1
4549.749	R(20)	0	1
4550.674	R(11)	0	1
4552.199	R(10)	0	1
4553.894	R(9)	0	1
4555.724	R(8)	0	1
4557.683	R(7)	0	1
4559.179	R(23)	0	1
4564.319	R(24)	0	1
4577.620	Q(7)	0	1
4578.077	Q(8)	0	1
4578.635	Q(9)	0	1
4579.298	Q(10)	0	1
4581.027	Q(12)	0	1
4582.137	Q(13)	0	1
4583.438	Q(14)	0	1
4584.971	Q(15)	0	1
4586.766	Q(16)	0	1
4588.867	Q(17)	0	1
4591.324	Q(18)	0	1
4594.202	Q(19)	0	1
4601.499	Q(21)	0	1
4606.100	Q(22)	0	1
4610.360	P(12)	0	1
4617.263	P(14)	0	1
4620.970	P(15)	0	1
4624.880	P(16)	0	1
4662.174	P(23)	0	1
4670.878	R(6)	1	2
4670.997	R(7)	1	2
4674.584	R(10)	1	2
4680.740	Q(1)	1	2
4682.196	Q(3)	1	2
4683.390	Q(4)	1	2
4686.794	Q(6)	1	2
4689.062	Q(7)	1	2
4689.123	P(3)	1	2
4691.768	Q(8)	1	2
4694.957	Q(9)	1	2
4696.381	P(5)	1	2
4700.498	P(6)	1	2
4704.958	P(7)	1	2
4708.188	Q(12)	1	2
4709.810	P(8)	1	2
4720.849	P(10)	1	2
4727.156	P(11)	1	2
4728.807	R(18)	1	2

Table A2. Calculated ExoMol AlH lines which are 'absent'/misplaced or severely blended in observed spectra of Proxima Cen. Diffuse and/or misplaced lines shown in Figs 4 and 5 are marked by itallic font.

Wavelength in air (Å)	Branch(j)	v'	v''
4073.714	R(10)	1	0
4076.959	R(11)	1	0
4080.976	R(12)	1	0
4085.867	R(13)	1	0
4091.767	R(14)	1	0
4092.018	Q(10)	1	0
4096.665	Q(11)	1	0
4098.824	R(15)	1	0
4107.223	R(16)	1	0
4108.092	Q(13)	1	0
4114.923	P(11)	1	0
4115.074	Q(14)	1	0
4121.648	P(12)	1	0
4123.066	Q(15)	1	0
4128.929	R(18)	1	0
4129.052	P(13)	1	0
4132.231	Q(16)	1	0
4137.233	P(14)	1	0
4142.750	Q(17)	1	0
4142.778	R(19)	1	0
4146.300	P(15)	1	0
4154.845	Q(18)	1	0
4156.394	P(16)	1	0
4159.068	R(20)	1	0
4167.670	P(17)	1	0
4168.770	Q(19)	1	0
4178.198	R(21)	1	0
4180.326	P(18)	1	0
4194.581	P(19)	1	0
4203.380	Q(21)	1	0
4210.708	P(20)	1	0
4224.836	Q(22)	1	0
4247.393	R(19)	0	0
4249.872	P(22)	1	0
4250.103	R(20)	0	0
4253.469	R(21)	0	0
4257.596	R(22)	0	0
4262.596	R(23)	0	0
4268.595	R(24)	0	0
4273.710	P(23)	1	0
4291.798	Q(20)	0	0
4296.604	Q(21)	0	0
4302.062	Q(22)	0	0
4308.269	Q(23)	0	0
4315.333	Q(24)	0	0
4323.449	Q(25)	0	0
4338.087	P(21)	0	0
4344.971	P(22)	0	0

Table A2 – *continued*

Wavelength in air (Å)	Branch(j)	v'	v''
4352.494	P(23)	0	0
4356.537	R(9)	1	1
4358.783	R(10)	1	1
4360.750	P(24)	0	0
4362.061	Q(3)	1	1
4365.504	R(12)	1	1
4369.916	P(25)	0	0
4370.204	R(13)	1	1
4379.745	Q(10)	1	1
4380.084	P(26)	0	0
4383.015	R(15)	1	1
4384.303	Q(11)	1	1
4389.565	Q(12)	1	1
4391.506	R(16)	1	1
4395.640	Q(13)	1	1
4401.700	R(17)	1	1
4402.649	Q(14)	1	1
4405.221	P(11)	1	1
4410.747	Q(15)	1	1
4412.078	P(12)	1	1
4413.878	R(18)	1	1
4419.644	P(13)	1	1
4420.107	Q(16)	1	1
4428.023	P(14)	1	1
4428.377	R(19)	1	1
4437.346	P(15)	1	1
4447.765	P(16)	1	1
4458.089	Q(19)	1	1
4459.467	P(17)	1	1
4465.957	R(21)	1	1
4472.664	P(18)	1	1
4487.620	P(19)	1	1
4504.632	P(20)	1	1
4524.063	P(21)	1	1
4546.325	P(22)	1	1
4547.079	R(18)	0	1
4548.122	R(19)	0	1
4552.060	R(21)	0	1
4555.164	R(22)	0	1
4571.896	P(23)	1	1
4580.092	Q(11)	0	1
4597.564	Q(20)	0	1
4611.468	Q(23)	0	1

Table A2 – *continued*

Wavelength in air (Å)	Branch(j)	v'	v''
4613.739	P(13)	0	1
4617.797	Q(24)	0	1
4625.171	Q(25)	0	1
4629.041	P(17)	0	1
4633.484	P(18)	0	1
4638.270	P(19)	0	1
4643.453	P(20)	0	1
4649.111	P(21)	0	1
4655.323	P(22)	0	1
4669.842	P(24)	0	1
4671.193	R(5)	1	2
4671.610	R(8)	1	2
4671.909	R(4)	1	2
4672.777	R(9)	1	2
4672.978	R(3)	1	2
4674.390	R(2)	1	2
4676.111	R(1)	1	2
4677.124	R(11)	1	2
4678.141	R(0)	1	2
4678.390	P(25)	0	1
4680.519	R(12)	1	2
4681.322	Q(2)	1	2
4684.904	R(13)	1	2
4684.908	Q(5)	1	2
4688.067	P(26)	0	1
4690.454	R(14)	1	2
4692.600	P(4)	1	2
4697.360	R(15)	1	2
4698.702	Q(10)	1	2
4703.077	Q(11)	1	2
4705.864	R(16)	1	2
4714.147	Q(13)	1	2
4715.087	P(9)	1	2
4716.236	R(17)	1	2
4721.005	Q(14)	1	2
4729.227	Q(15)	1	2
4734.097	P(12)	1	2
4738.723	Q(16)	1	2
4741.767	P(13)	1	2
4743.949	R(19)	1	2
4749.827	Q(17)	1	2
4750.294	P(14)	1	2

Table A3. HJ lines shown in Fig. 7. Here, $\lambda_{\rm air}^{\rm adjusted}$ is corrected by $\Delta\lambda$ line wavelength in air, $gf = g_l \times f_{li}$, E'' energy of the lower level, $\gamma_R^{\rm ExoMol} = 1/\tau_{\rm upper} + 1/\tau_{\rm lower}$ – theoretical radiative damping constant calculated from the lifetimes of the upper ($\tau_{\rm upper}$) and lower ($\tau_{\rm lower}$) levels provided by ExoMol, $\gamma_R^{\rm adjusted}$ adjusted value from comparison with observations, Ident, v', and v'' are identifications of the line branch transition, upper, and lower vibrational numbers, respectively.

$\lambda_{\rm air}^{\rm adjusted}$	$\Delta\lambda$	gf	E''	$\log(\gamma_R^{\rm ExoMol})$	$\log(\gamma_R^{\rm adjusted})$	Ident	v'	v''
4290.556		3.988E-01	0.102	7.170		P(11)	0	0
4291.858	0.04	1.288E + 00	0.320	7.073	10.5	Q(20)	0	0
4294.175		4.336E-01	0.121	7.166		P(12)	0	0
4296.801	0.28	1.295E + 00	0.351	7.058	11.0	Q(21)	0	0
4297.975		4.668E-01	0.141	7.160		P(13)	0	0
4301.973		4.982E-01	0.162	7.154		P(14)	0	0
4302.486	0.42	1.133E + 00	0.384	6.983	11.5	Q(22)	0	0
4306.193		5.275E-01	0.185	7.147		P(15)	0	0
4309.054	0.78	1.185E + 00	0.418	6.993	12.2	Q(23)	0	0
4310.662		5.543E-01	0.209	7.139		P(16)	0	0
4316.898	1.39	1.060E + 00	0.453	6.929	12.5	Q(24)	0	0
4315.412		5.783E-01	0.235	7.130		P(17)	0	0
4320.481		5.989E-01	0.262	7.120		P(18)	0	0
4323.449		9.137E-01	0.489	6.869		Q(25)	0	0
4325.911		6.155E-01	0.290	7.108		P(19)	0	0
4331.761		6.272E-01	0.320	7.095		P(20)	0	0
4338.087		6.249E-01	0.351	7.073		P(21)	0	0
4344.971		6.295E-01	0.384	7.058		P(22)	0	0
4352.494		5.521E-01	0.418	6.983		P(23)	0	0

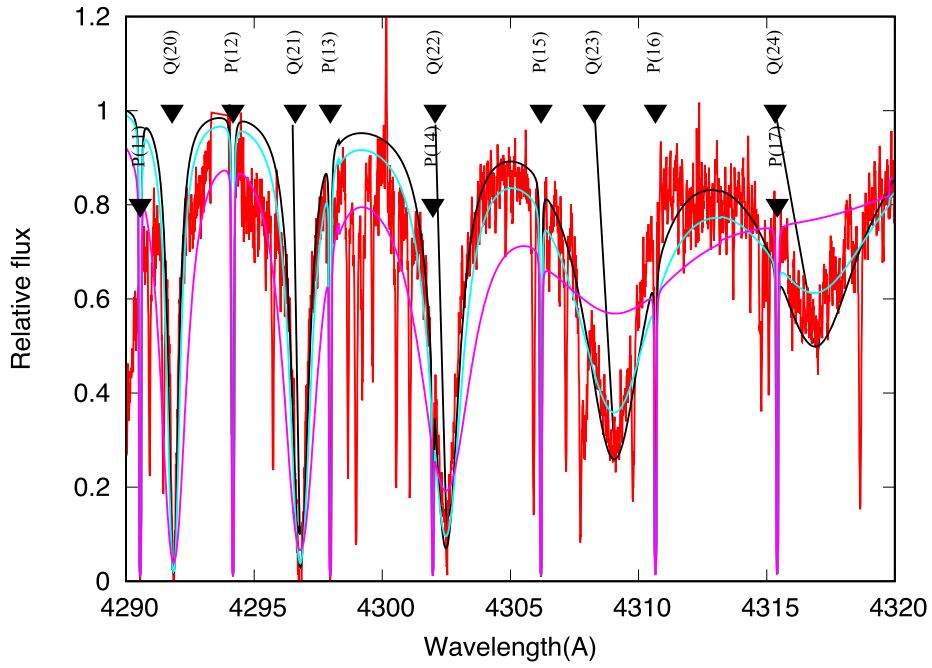

Figure A1. Fit to broadened HJ lines of AlH with parameters shown in Table A3 to the observed Proxima Cen spectrum. Black, cyan, and pink lines show the cases of γ_R, $\gamma_R \times 1.02$ and $\gamma_R \times 1.05$, respectively. Here, $K_x = 80$, [Al/Fe] $= -0.1$. Arrows show the 'true' positions of some AlH lines from the Q branch of (1-0) band.

This paper has been typeset from a TEX/LATEX file prepared by the author.